Supplementary Information

Rational Rock-salt Phase Engineering of Nickel-rich Layered Cathode Interface for Enhanced Rate and Cycling Stability

Wenjie Wang[a,‡], Yanke Shi[a,‡], Pengfei Li[a], Ruiqing Wang[b], Fei Ye[b], Xiaoyu Zhang[a], Wei Li[b], Zhuosen Wang[a], Chunyang Xu[a,*], Dongqing Xu[c], Qun Xu[a], Xinwei Cui[a,*]

[a] Henan Institute of Advanced Technology, Zhengzhou University, Zhengzhou, Henan 450003, P. R. China.

[b] Xinxiang Tianli Lithium Energy Co., Ltd., Xinxiang, Henan 453000, P. R. China.

[c] School of Life and Health Science, Anhui Science and Technology University, Fengyang, Anhui 233100, China.

‡ These authors contribute equally to this work.

* E-mails: xinweic@zzu.edu.cn; chunyangxu@zzu.edu.cn

Materials and Methods

Materials synthesis

For the synthesis of $LiNi_{0.83}Co_{0.12}Mn_{0.05}O_2$ (pristine NCM83), the precursor of $Ni_{0.83}Co_{0.12}Mn_{0.05}(OH)_2$ (purchased from Xinxiang Tianli Lithium Energy Co., Ltd, Henan, China) was mixed with appropriate amounts of $LiOH{\cdot}H_2O$ (aladdin, 99%) (Li:M molar ratio = 1.03:1). The mixture was calcined at 500 ºC for 6 h and then heated at 780 ºC for 12 h in pure oxygen environment (O_2 purity$\geqslant$99.999%). The heating rate was set to be 3 ºC min^{-1}. 5 g of pristine NCM83 secondary particles were added to 25 mL of 1.2 mg mL^{-1} aluminum glycinate (aladdin, 97%) aqueous solution and the mixture was stirred with a magnetic stirrer at 300 rpm for 10 min. After filtration, the samples were dried at 100 ºC for 10 h under vacuum, and then calcined at 700 ºC in pure oxygen environment for 4 h to obtain NCM83-Al-N. For the preparation of water-washed NCM83, 5 g pristine NCM83 particles were added to 25 mL deionized water, followed by the magnetic stirring at 300 rpm for 2 min and vacuum drying at 100 ºC for 10 h. To prepare NCM83-Al, the pristine NCM83 particles were mixed with 0.23 wt.% γ-Al_2O_3 nanoparticles and calcined at 700 ºC for 4 h in pure oxygen environment. Then, 5 g of as-treated samples were added to 25 mL deionized water. The mixture was stirred with a magnetic stirrer at 300 rpm for 2 min and then dried at 100 ºC for 10 h under vacuum.

Materials Characterization

Morphology and elemental mapping of the cathode particles were characterized by a field-emission scanning electron microscopy using a GeminiSEM 300 (ZEISS), equipped with energy dispersive X-ray spectroscopy (EDX) (Smart EDX of SE2). To observe the cross-sectional SEM image of the secondary particles, the electrodes were cut using an ion beam cutting system (Leica EM TIC3X). The microstructural analyses were taken by transmission electron microscopy (TEM) and high-resolution TEM (HRTEM) at 200 kV (JEOL JEM 2100F). Atomic-scale high angle

annular dark field scanning transmission electron microscope (HAADF-STEM) images were acquired by the aberration corrected JEM-ARM300F at the operation voltage of 300 kV. Before HAADF-STEM measurements, a randomly selected secondary particle was cut into a slice by focused ion beam (FIB, Crossbeam 350, ZEISS). The chemical compositions were measured by inductively coupled plasma atomic emission spectroscopy (ICP-AES, PE Avio 200). Powder X-ray diffraction (XRD) patterns were performed on a Bruker D8 Advance X-ray diffractometer at a slow scan rate of 1° min^{-1}, with a Cu-sealed tube (λ= 0.15418 nm) at 40 kV and 40 mA. X-ray photoelectron spectroscopy (XPS) was conducted using the Thermo Fisher Scientific ESCALAB 250Xi instrument. The base pressure was maintained about 1 × 10^{-9} mbar, and the excitation source was employed by Al Kα X-ray radiation (hv=1486.68 eV) with a spot size of 500 μm. For XPS depth profiles, Ar-ion sputtering was taken for 10 s, 20 s, 40 s, 90 s, and 190 s with ion energy of 1 keV, prior to XPS analysis. The lithium impurity residual contents were determined by the chemical titration method with HCl on an INESA PHS-3C instrument. Time-of-flight secondary ion mass spectrometry (TOF-SIMS) analysis (PHI nanoTOF II Time-of-Flight SIMS) were employed via a pulsed 30 keV Bi_3^{++} as a primary ion beam. The sputter rate is 16 nm min^{-1} which was applied for scanning on an area of 100 μm × 100 μm of the sample surface.

Electrochemical Measurements

The slurries of the cathodes were prepared by mixing 80 wt.% active materials with 10 wt.% Super P and 10 wt.% polyvinylidene fluoride in N-methyl-2-pyrrolidinone. After the mixing, the slurry was coated onto Al foils with a mass loading level of ~3 mg cm^{-2} and dried at 120 ºC under vacuum overnight to remove the solvent. Then, the electrodes were punched into a disk with 12 mm in diameter and assembled into CR2032 coin cells. Lithium foil, Celgard PP2400, and 1 M $LiPF_6$ in ethylene carbonate (EC) /ethyl-methyl carbonate (EMC) (3:7; v:v) with 2 wt.% vinylene carbonate (VC) were served as the reference/counter electrode, separator, and electrolyte, respectively. The

four-point probe test (ROOKO FT-345) was used to study the electrical conductivity. *In-situ* differential electrochemical mass spectroscopy (DEMS) measurements were conducted on a commercial quadrupole mass spectrometer (Hiden HPR-40). Galvanostatic charge/discharge cycling was performed on a Xinwei CT-4008Q battery testing system with the voltage range of 3.0 ~ 4.3 V (*vs*. Li/Li^+) at 25 ℃. Electrochemical impedance spectroscopy (EIS) was performed using a Bio-Logic VSP-3e chassis-8 slots electrochemical workstation (amplitude voltage: 5 mV, frequency range: 1 mHz ~ 100 kHz). The galvanostatic intermittent titration technique (GITT) was employed at a constant-current condition of 0.1C for 30 min, followed by a rest interval for 4 h. The D_{Li^+} based on GITT test can be calculated from the following equation (Equation S1):[1]

$$D_{Li^+} = \frac{4}{\pi\tau}\left(\frac{n_m V_m}{S}\right)^2\left(\frac{\Delta E_S}{\Delta E_\tau}\right)^2 \quad \left(\tau << \frac{L^2}{D_{Li^+}}\right) \quad \text{(S1)}$$

where τ is the time duration of the pulse, n_m is the molar mass of active material, V_m is the molar volume of the active material, S is the cell interfacial area, ΔE_s and ΔE_τ is the voltage changes brought by pulse and constant current, respectively, and L is the length of Li^+ diffusion.

The content of residual lithium was determined via the electrochemical titration method. 20 mL standard hydrochloric acid solution (1 mol L^{-1}) was first diluted in a 1000 mL volumetric flask. Then, 20 mL sodium carbonate standard solution (0.01 mol L^{-1}) was used to calibrate the actual concentration of the diluted hydrochloric acid solution. In the next step, 1 g of particle samples were added into 20 mL deionized water and stirred for 40 minutes. Finally, the mixture was filtered and the 10 mL filtrate was titrated with the calibrated hydrochloric acid solution by a potentiometric titrator (LEICI PHS-3C).

First-Principles Calculations

Vienna Ab Initio Simulation Package (VASP) was applied to conduct the first-principle calculation,[2,3] using a generalized gradient approximation (GGA) of exchange-correlation

functional in the Perdew, Burke, and Ernzerhof (PBE) form.[4,5] A plane-wave energy cut off of 480 eV was used together with norm-conserving pseudopotentials, and Γ-centered 3 × 3 × 3 k-point was applied correspondingly. 3 × 3 × 1 supercells of $LiNiO_2$ (space group: *R-3m*) and 2 × 2 × 2 supercells of NiO (space group: *Fm-3m*) structures were applied. To construct doped or co-doped supercells, different stoichiometries of Al atoms and N atoms were used to replace Ni and O, respectively, in either $LiNiO_2$ or NiO supercells. van der Waals corrections were considered by using the DFT-D3 method of Grimme.[6,7] Spin polarization was taken into consideration and the ferromagnetic configuration was set as the initial magnetic structure. The DFT+U method was also used to account for the strong correlation in the calculations.[8,9] The Hubbard U parameter of Ni was 5.77 eV.[10] An energy of 1×10^{-6} eV and a force of 0.01 eV $Å^{-1}$ were set for geometry optimizations.

The formation energy of oxygen-vacancy (V_o) was defined as

$$E_f(V_O) = E(V_O) - E(pristine) + \frac{1}{2}E(O_2)$$

where $E(V_o)$ and E(pristine) are the total energies of the oxygen-deficient and the pristine structures, respectively. $E(O_2)$ is the energy of an oxygen molecule. Because the chemical potential of oxygen gas is dependent on the temperature and DFT normally overestimates the oxygen binding energy, a −1.36 eV energy correction for the O_2 molecule was used in all calculations to correct the self-interaction errors within DFT.[11]

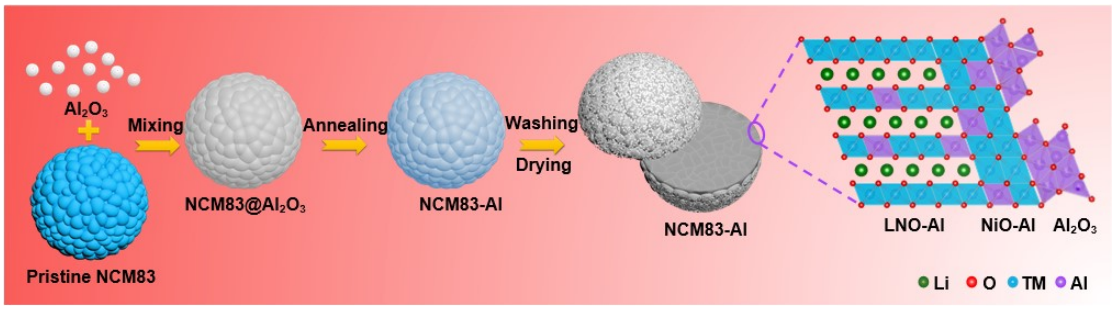

Fig. S1 The synthesis route with the illustration of the interface structure of NCM83-Al.

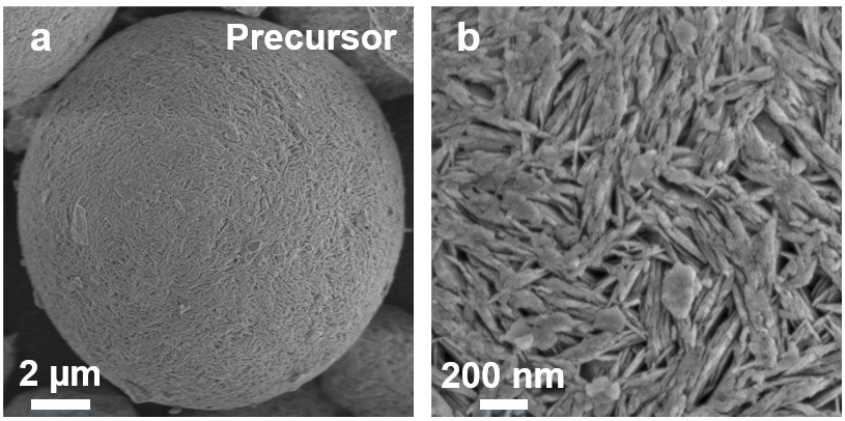

Fig. S2 SEM images of the $Ni_{0.83}Co_{0.12}Mn_{0.05}(OH)_2$ precursor. (a) Secondary particle. (b) Primary particles.

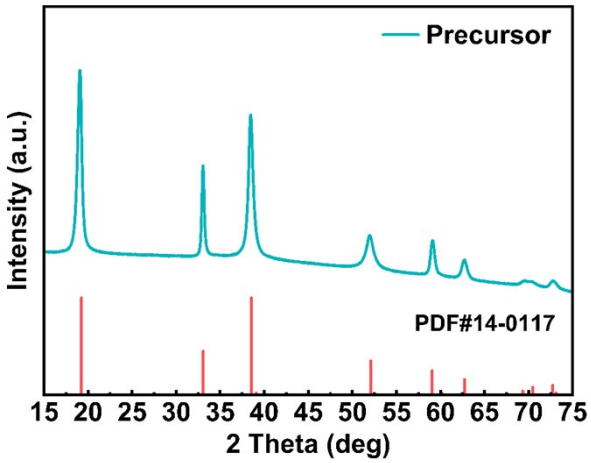

Fig. S3 XRD pattern of the $Ni_{0.83}Co_{0.12}Mn_{0.05}(OH)_2$ precursor.

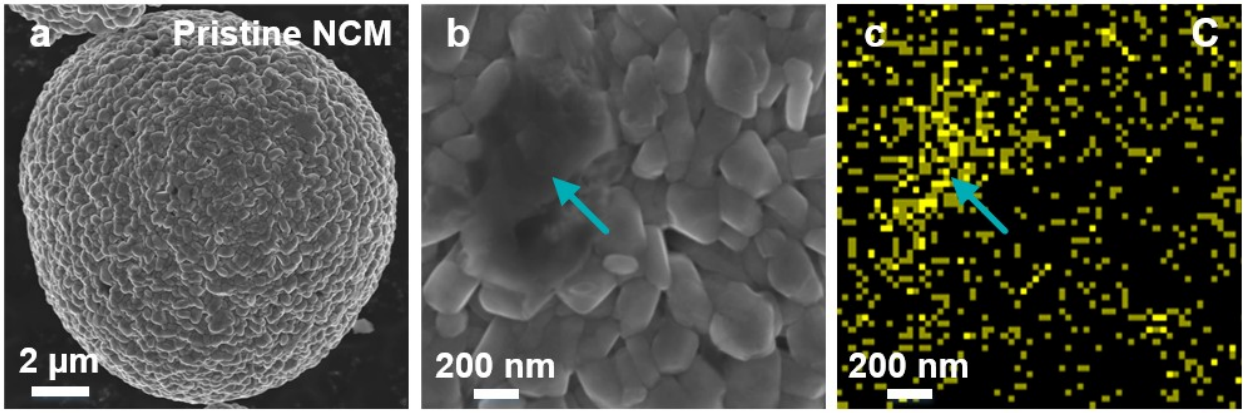

Fig. S4 SEM images of pristine NCM83. (a) Secondary particle. (b) Primary particles. (c) The corresponding elemental mappings of C.

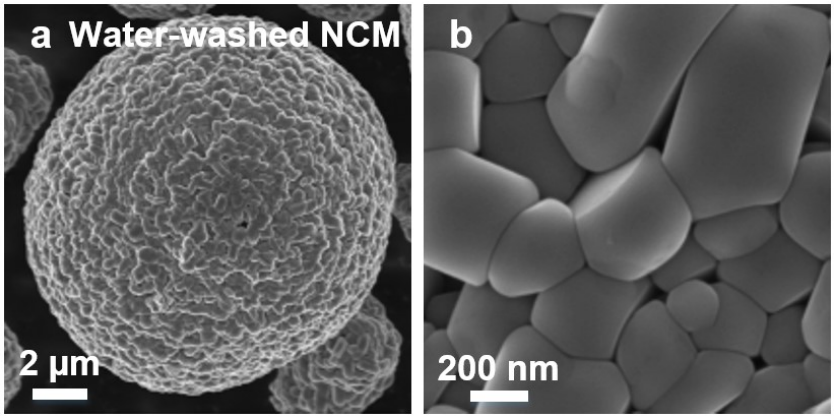

Fig. S5 SEM images of water-washed NCM83. (a) Secondary particle. (b) Primary particles.

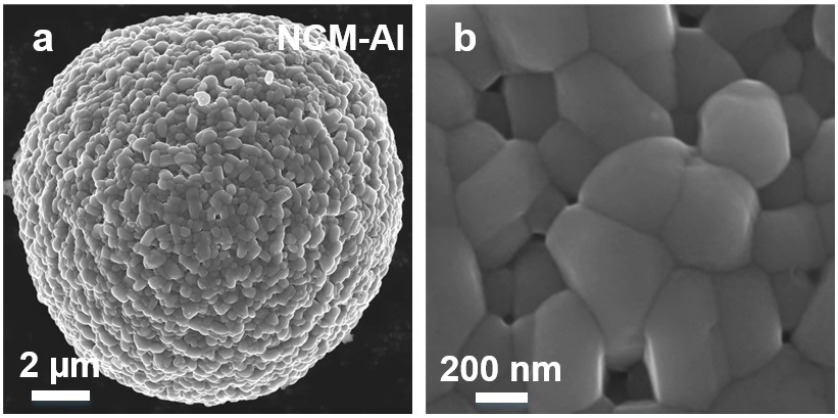

Fig. S6 SEM images of NCM83-Al. (a) Secondary particle. (b) Primary particles.

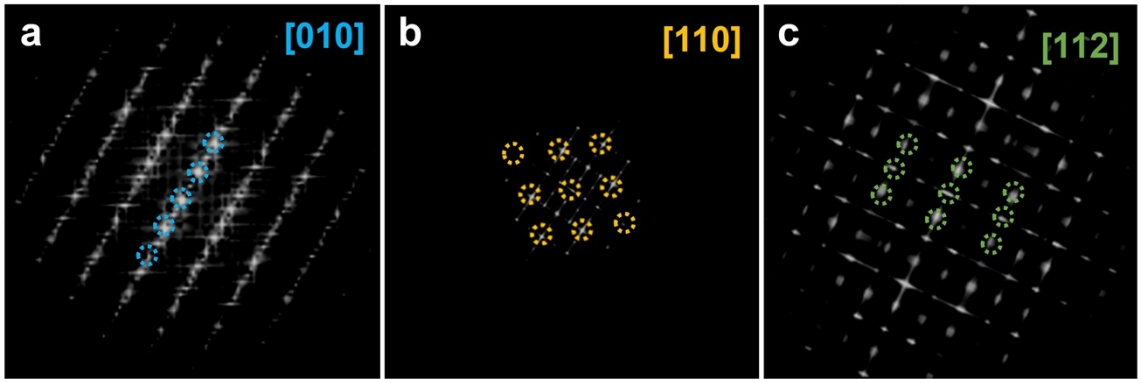

Fig. S7 Simulated FFT images of the inner layered structure (a), the interlayer rock-salt phase (b), and the outer Al_2O_3-based inert coating (c).

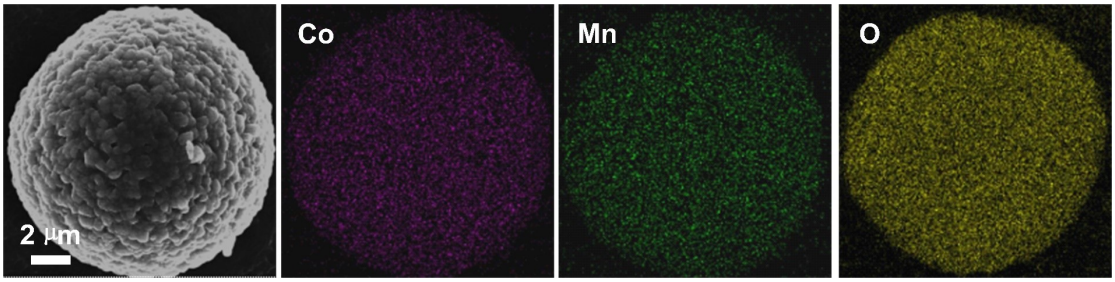

Fig. S8 SEM image of NCM83-Al-N and the corresponding elemental mappings of Co, Mn, and O.

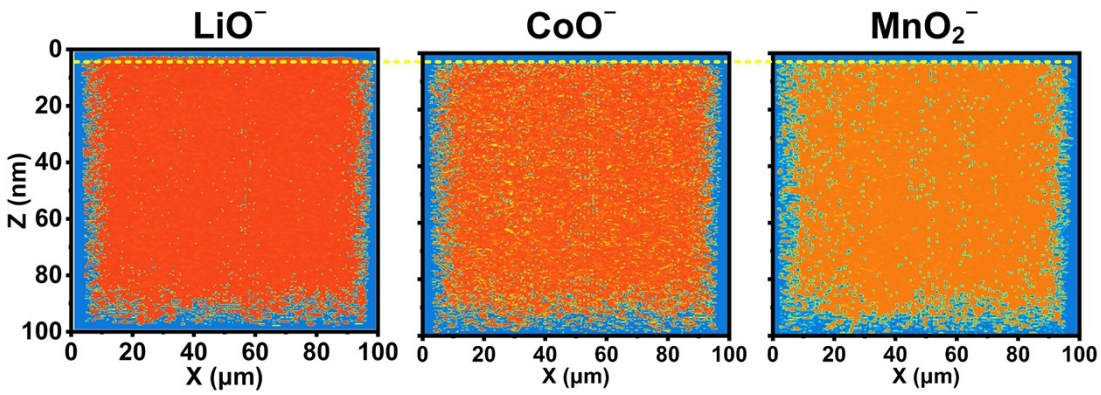

Fig. S9 TOF-SIMS diagrams showing 2D depth distribution of LiO^-, CoO^- and MnO_2^- across the interface of NCM83-Al-N. The white dashed lines correspond to the interface between the rock-salt phase and the internal layered structure.

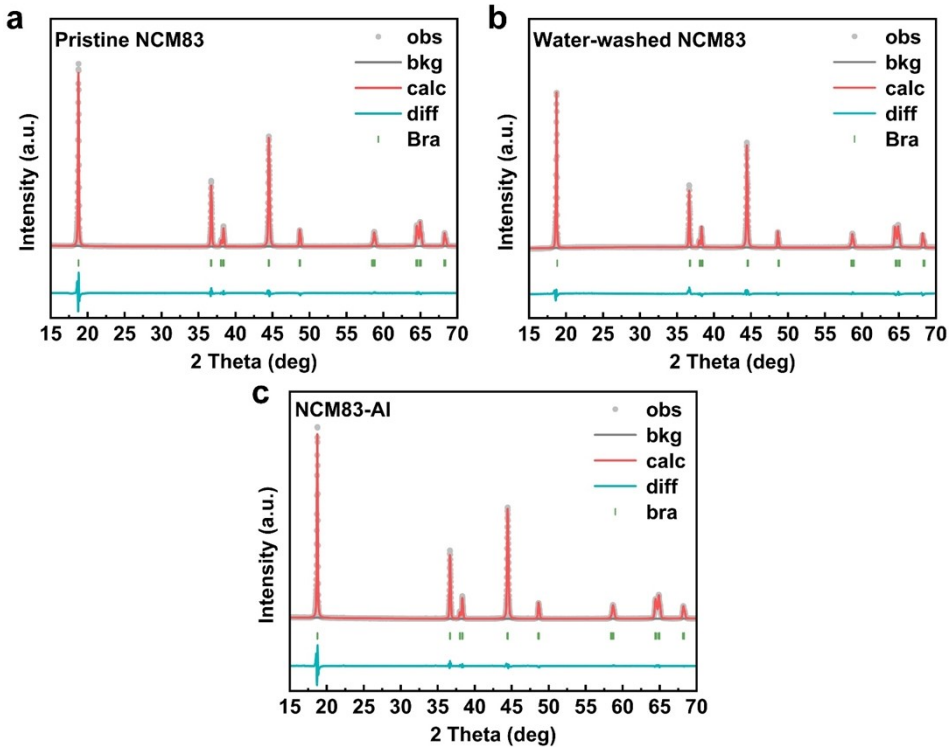

Fig. S10 XRD Rietveld Refinements of (a) pristine NCM83, (b) water-washed NCM83, and (c) NCM83-Al.

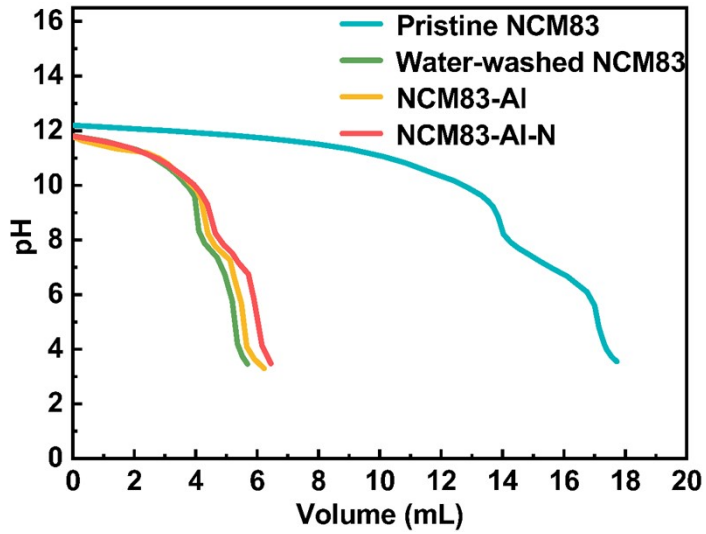

Fig. S11 The electrometric titration curves, illustrating the amount of residual lithium compounds present on the surface of pristine NCM83, water-washed NCM83, NCM83-Al, and NCM83-Al-N,

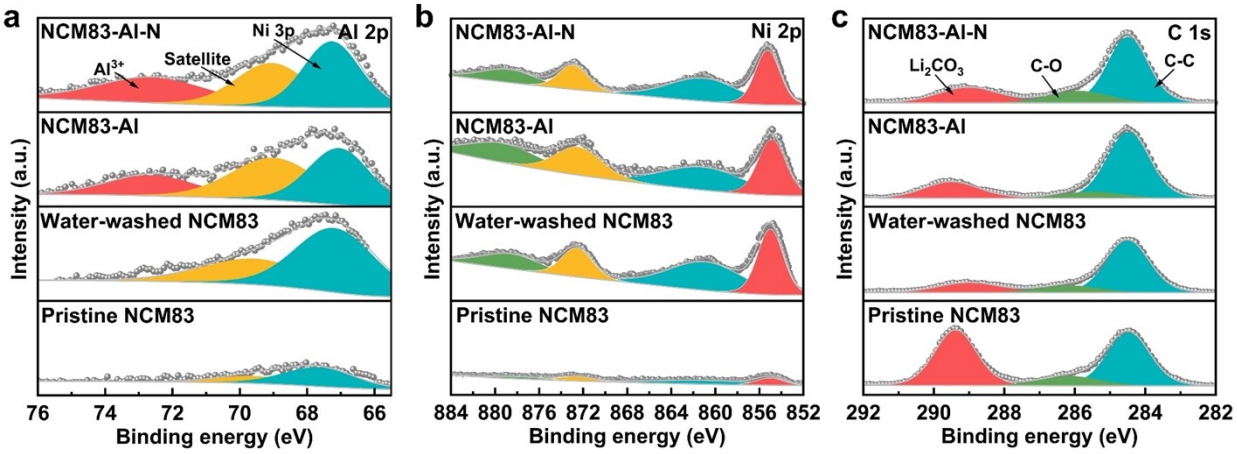

Fig. S12 XPS spectra of (a) Al 2*p*, (b) Ni 2*p*, and (c) C 1*s* for pristine NCM83, water-washed NCM83, NCM83-Al, and NCM83-Al-N.

High-resolution XPS was conducted to compare the surface chemical valence states of all four samples. Both the Al 2*p* and Ni 3*p* peaks are situated in the region between 77.0 and 65.0 eV, (Fig. S12a), while the signals located at about 74.0 eV correspond to the Al–O bond, which can be ascribed to the Al_2O_3 coating and Al^{3+} doping in NCM83-Al and NCM83-Al-N, as also shown in Fig. 2. It is noteworthy that the signals of Ni 2*p* signals in pristine NCM83 is extremely weak, revealing that pristine NCM83 possessed large amounts of residual lithium. This can be further proved by C 1*s* spectra in Fig. S12c. Only pristine NCM83 shows strong CO_3^{2-} peak at around 289.7 eV for pristine NCM83, consistent with the electrometric titration results in Fig. 3b and S11.

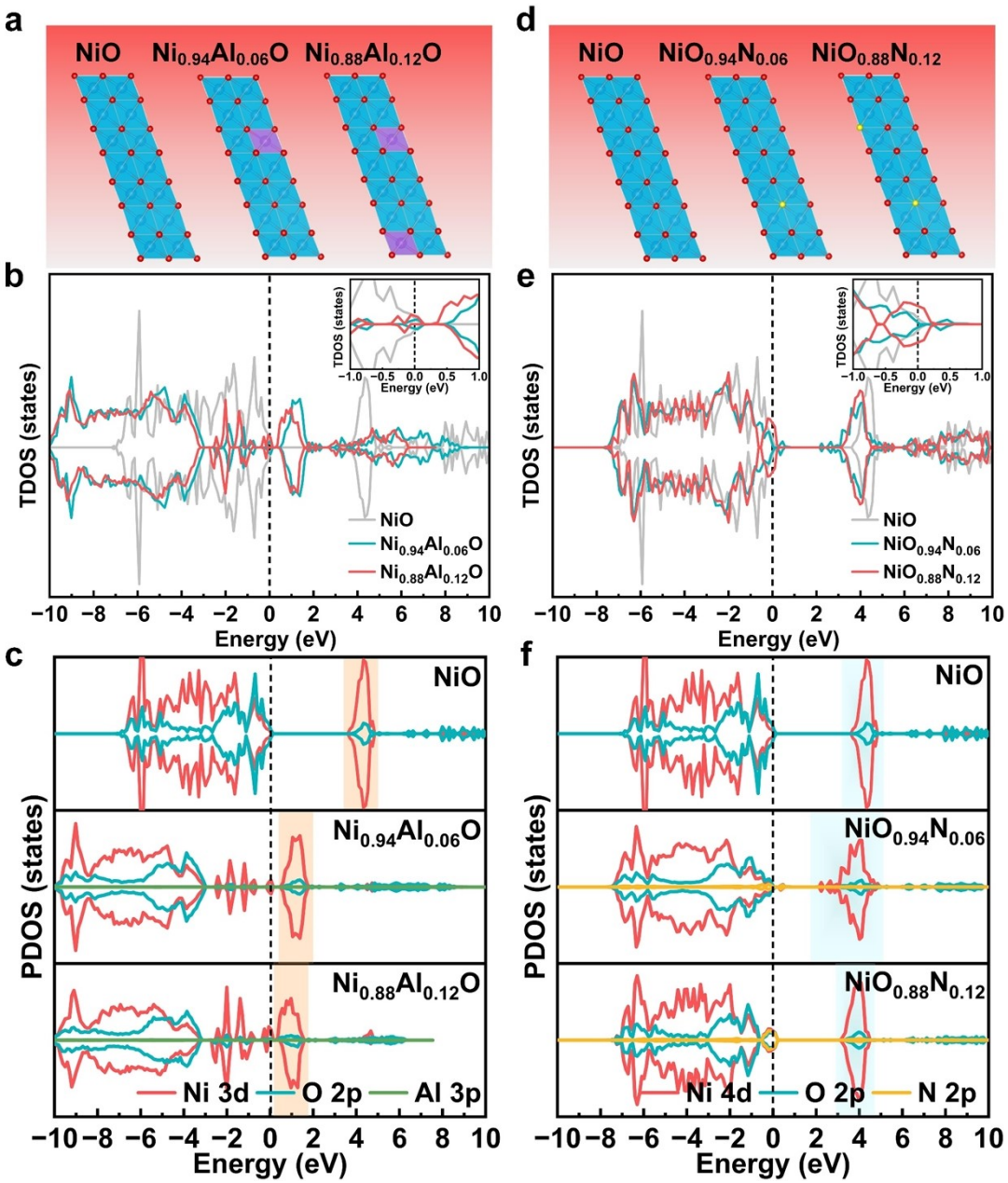

Fig. S13 Change of DOS diagrams for different doping levels of Al and N in the rock-salt phase. (a-c) Supercells of NiO-Al, with different levels of Al doping (a), with the comparison of their TDOS (b) and PDOS (c) diagrams. (d-f) Supercells of NiO-N, with different levels of N doping (d), with the comparison of their TDOS (e) and PDOS (f) diagrams.

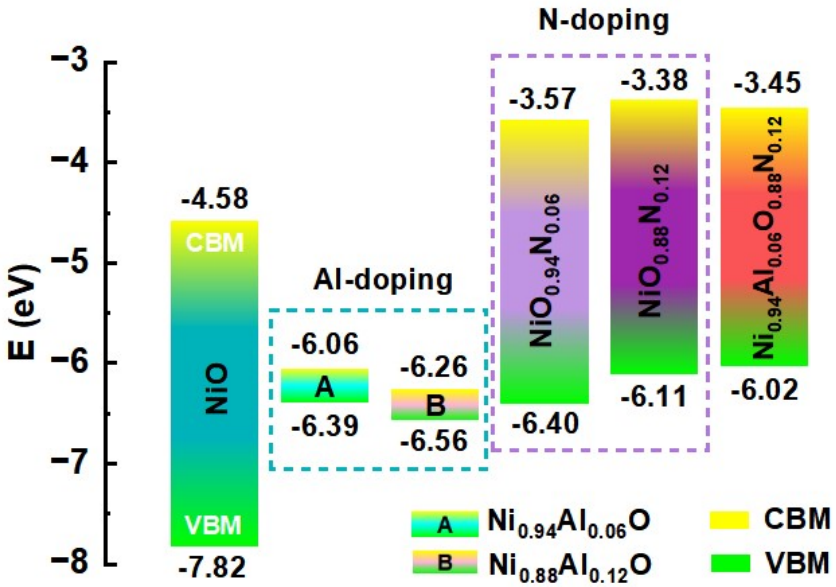

Fig. S14 The relative positions of valence band maximun (VBM) and conduction band minimum (CBM) for different doping chemistries in the rock-salt phase.

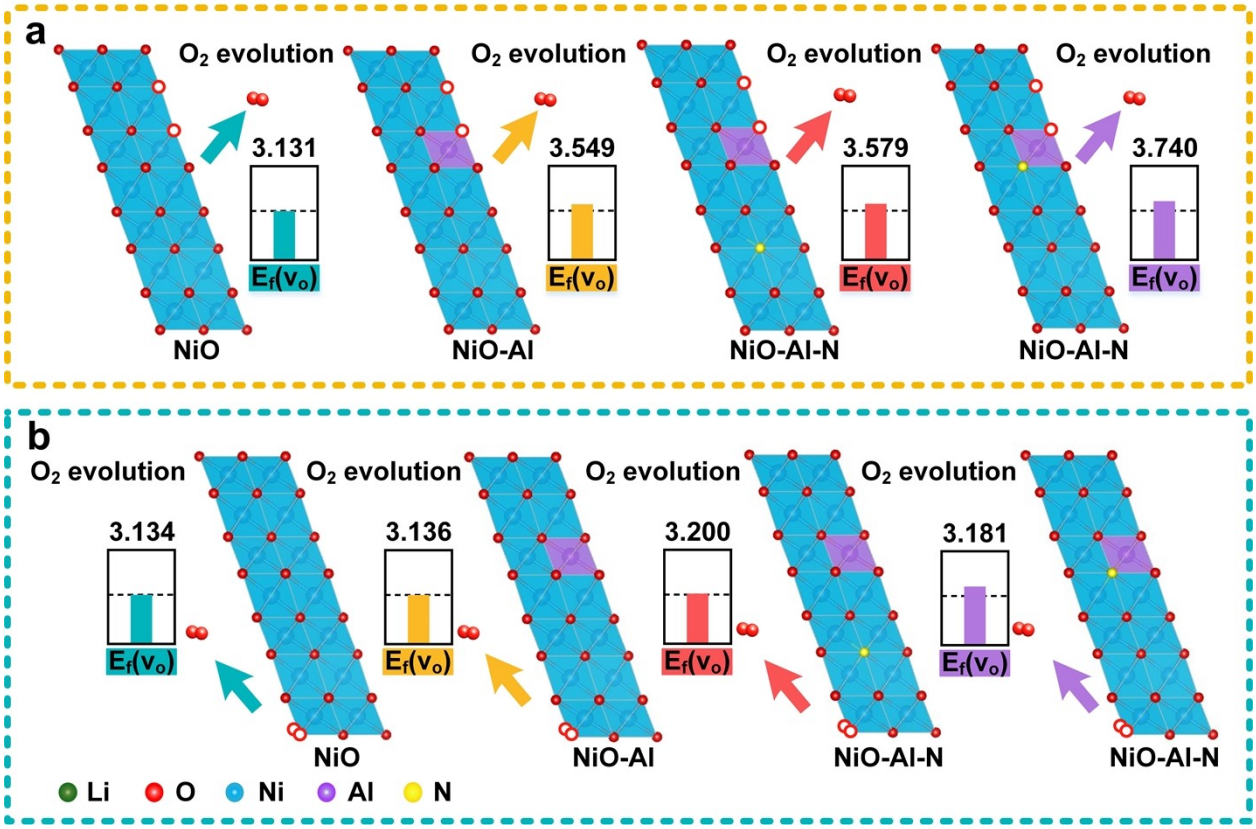

Fig. S15 Oxygen-vacancy (V_o) formation energies in the rock-salt phase of pure NiO, NiO-Al, and NO-Al-N. (a) Oxygen vacancies one lattice away from the Al doped site. (b) Oxygen vacancies away from the Al doped site.

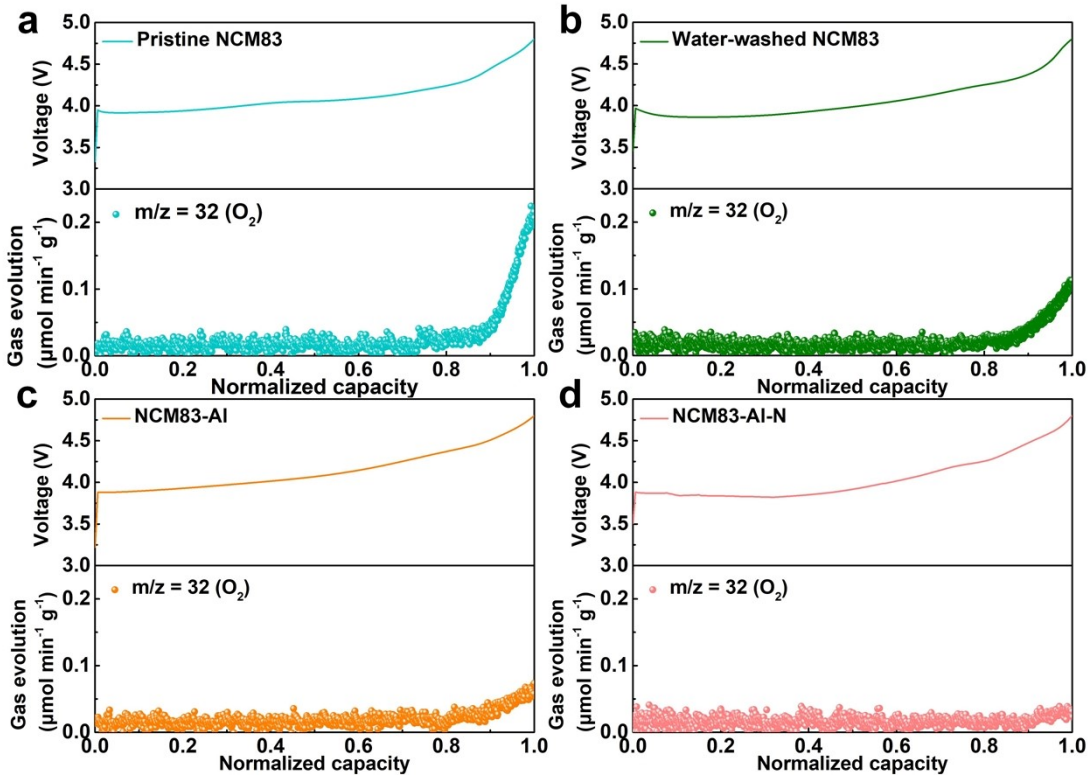

Fig. S16 O_2 evolution analysis of pristine NCM83 (a), water-washed NCM83 (b), NCM83-Al (c), and NCM83-Al-N (d) through *in-situ* DEMS.

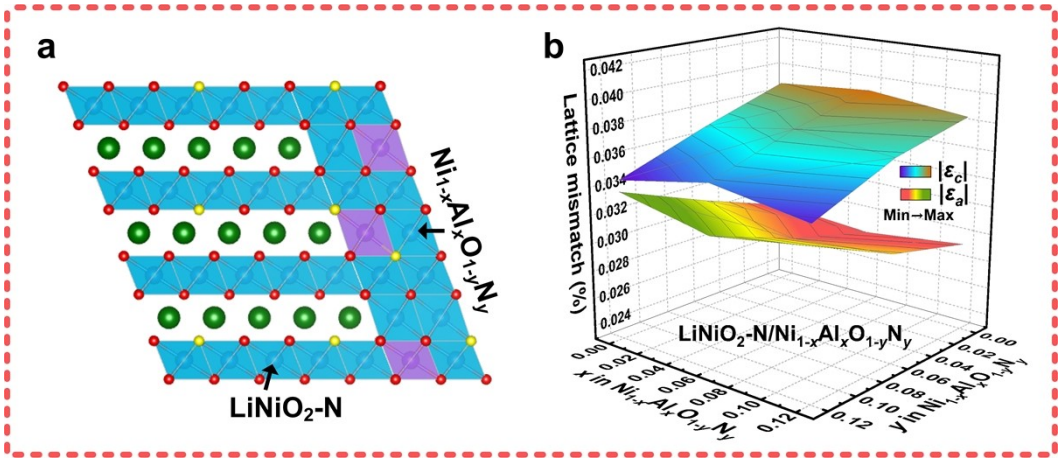

Fig. S17 Lattice mismatch of $LiNiO_2$-N/$Ni_{1-x}Al_xO_{1-y}N_y$ with varied Al doping (x) and N doping (y) levels in the rock-salt phase. (a) Interface model for $LiNiO_2$-N/$Ni_{1-x}Al_xO_{1-y}N_y$. (b) The corresponding lattice mismatch in the c-direction ($|\varepsilon_c|$) and a-direstion ($|\varepsilon_a|$) for $LiNiO_2$-N/$Ni_{1-x}Al_xO_{1-y}N_y$.

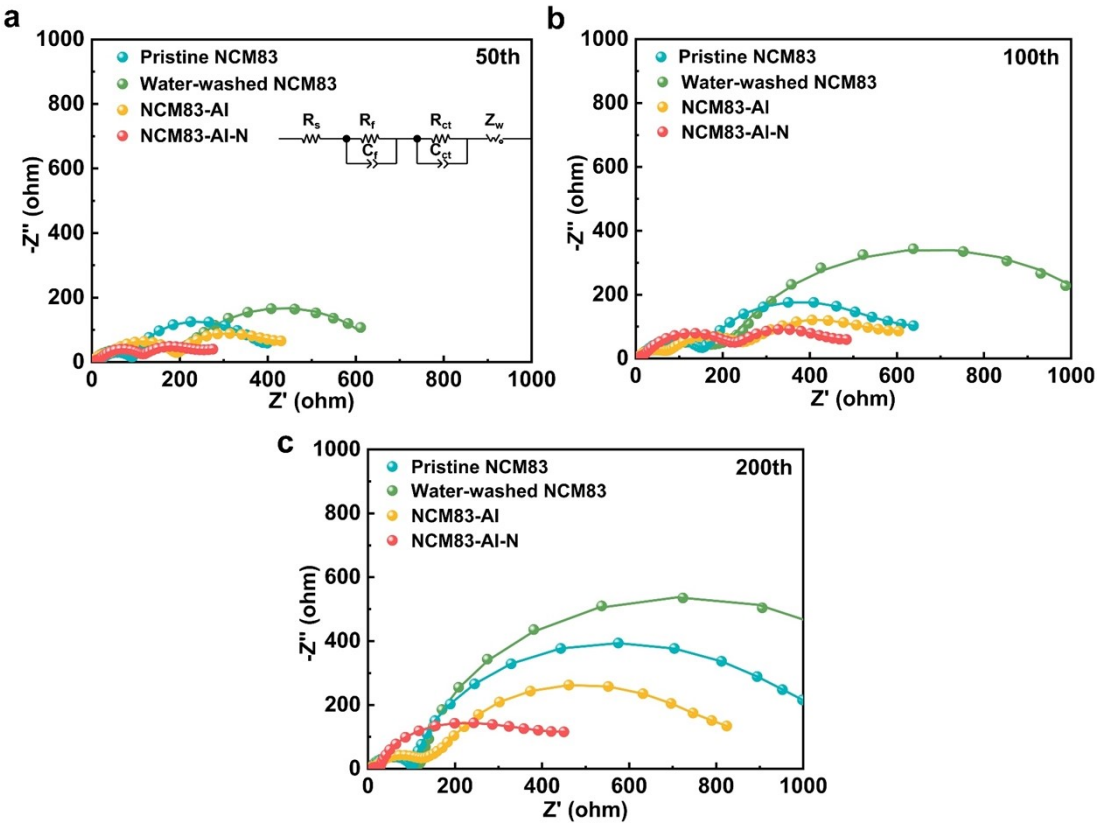

Fig. S18 Nyquist plots of pristine NCM83, water-washed NCM83, NCM83-Al, and NCM83-Al-N after (a) 50, (b) 100, and (c) 200 cycles. The insert in (a) is the equivalent circuit.

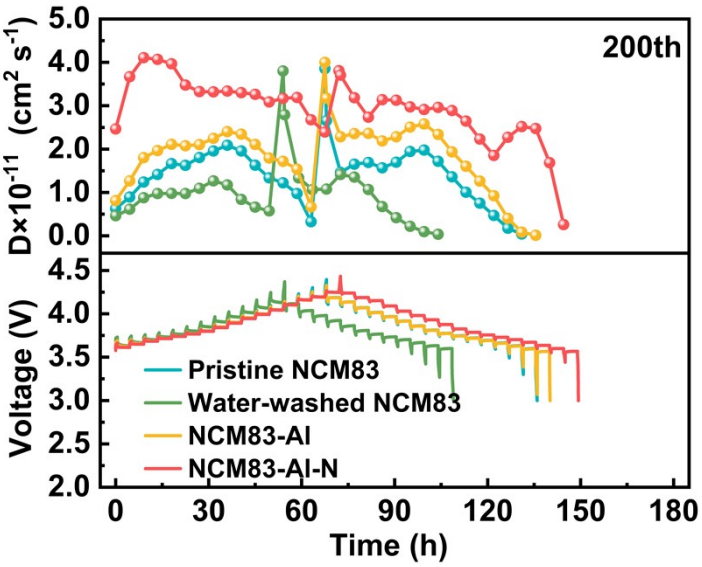

Fig. S19 GITT profiles and D_{Li}^{+} calculated from GITT profiles of pristine NCM83, water-washed NCM83, Al-NCM83, and Al-NCM83-N after 200 cycles.

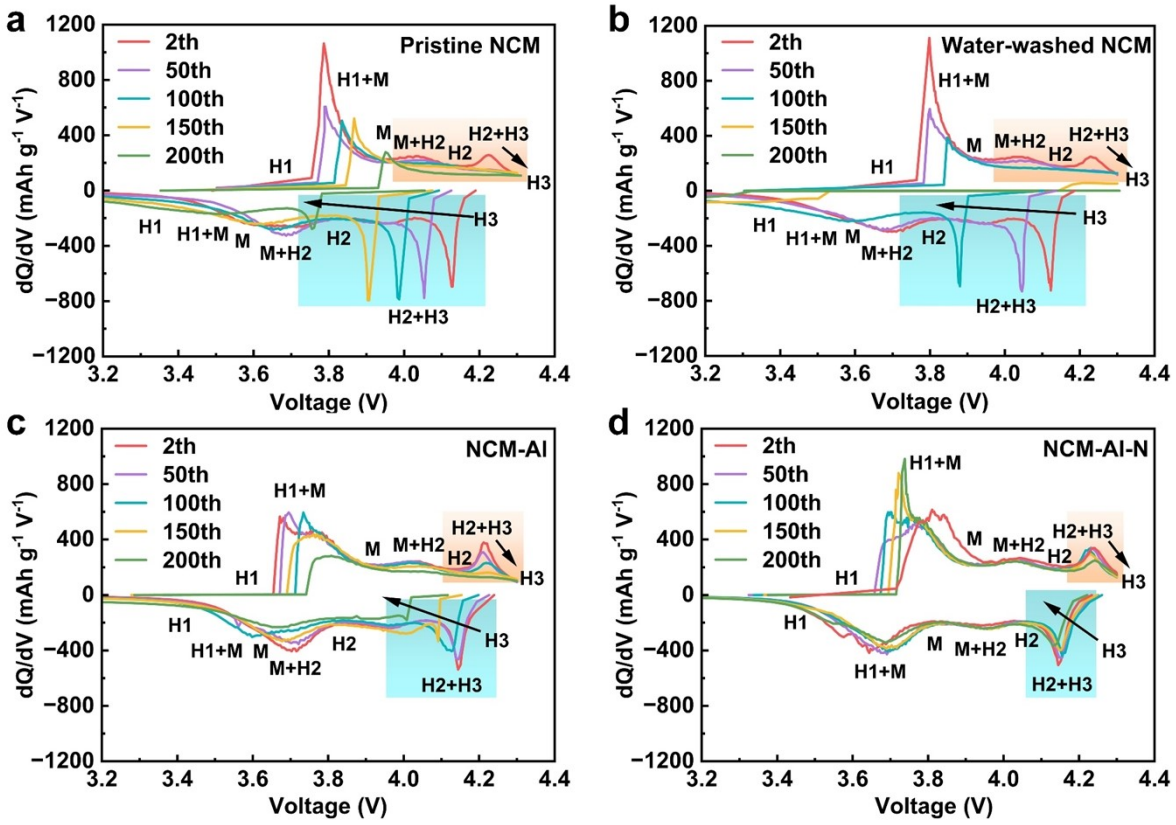

Fig. S20 The dQ/dV curves of (a) pristine NCM83, (b) water-washed NCM83, (c) NCM83-Al, and (d) NCM83-Al-N along cycles.

Table S1. Chemical compositions of the pristine NCM83, NCM83-Al, and NCM83-Al-N cathodes by ICP-AES analysis.

Cathode	ICP-AES (wt.%)			
	Ni	Co	Mn	Al
Pristine NCM83	47.550	6.749	2.684	/
NCM83-Al	48.660	6.901	2.741	0.107
NCM83-Al-N	48.715	6.899	2.737	0.042
Cathode	**Measured molar ration (%)**			
	Ni	**Co**	**Mn**	**Al**
Pristine NCM83	83.22	11.77	5.01	/
NCM83-Al	82.91	11.71	4.99	0.39
NCM83-Al-N	83.13	11.73	4.98	0.16

Table S2. The Rietveld-refined XRD results of pristine NCM83, water-washed NCM83, NCM83-Al, and NCM83-Al-N secondary particles.

Materials	a/b(Å)	c(Å)	c/a	V(Å^3)	Ni in Li (%)	h_{Li-O}(Å)	h_{TM-O}(Å)
Pristine NCM83	2.8688	14.1837	4.9441	101.09	2.77	2.0969	1.9762
Water-washed NCM83	2.8692	14.1804	4.9423	101.09	4.79	2.0766	1.9946
NCM83-Al	2.8739	14.2072	4.9435	101.62	3.43	2.1049	1.9758
NCM83-Al-N	2.8762	14.2181	4.9434	101.86	2.40	2.1036	1.9739

$h_{Li-O} = 2[1/3-Z_{ox}]c$

$h_{M-O} = c/3-(h_{Li-O})$

Table S3. Crystallographic data of pristine NCM83 determined from Rietveld refinement of XRD pattern.

Pristine $Ni_{0.83}Co_{0.12}Mn_{0.05}O_2$	Space group: R-3m		R_{wp}=1.68%		
Atom	x	y	z	Occupancy	Uiso
Li1	0.0	0.0	0.0	0.9723	0.01715
Ni1	0.0	0.0	0.500	0.8045	0.00123
Co1	0.0	0.0	0.500	0.1176	0.00123
Mn1	0.0	0.0	0.500	0.0502	0.00123
O1	0.0	0.0	0.243	1.0000	0.01923
Li2	0.0	0.0	0.500	0.0277	0.00123
Ni2	0.0	0.0	0.0	0.0277	0.01715

Table S4. Crystallographic data of water-washed NCM83 determined from Rietveld refinement of XRD pattern.

Water-washed $LiNi_{0.83}Co_{0.12}Mn_{0.05}O_2$	Space group: R-3m		R_{wp}=2.44%		
Atom	x	y	z	Occupancy	Uiso
Li1	0.0	0.0	0.0	0.9521	0.04399
Ni1	0.0	0.0	0.500	0.7849	0.00200
Co1	0.0	0.0	0.500	0.1174	0.00200
Mn1	0.0	0.0	0.500	0.0498	0.00200
O1	0.0	0.0	0.245	1.0000	0.02287
Li2	0.0	0.0	0.500	0.0479	0.00200
Ni2	0.0	0.0	0.0	0.0479	0.04399

Table S5. Crystallographic data of NCM83-Al determined from Rietveld refinement of XRD pattern.

NCM83-Al	Space group: R-3m		R_{wp}=1.55%		
Atom	x	y	z	Occupancy	Uiso
Li1	0.0	0.0	0.0	0.9657	0.00982
Ni1	0.0	0.0	0.500	0.7948	0.00503
Co1	0.0	0.0	0.500	0.1171	0.00503
Mn1	0.0	0.0	0.500	0.0499	0.00503
Al1	0.0	0.0	0.500	0.0039	0.00503
O1	0.0	0.0	0.242	1.0000	0.02744
Li2	0.0	0.0	0.500	0.0343	0.00503
Ni2	0.0	0.0	0.0	0.0343	0.00982

Table S6. Crystallographic data of NCM83-Al-N determined from Rietveld refinement of XRD pattern.

NCM83-Al-N	Space group: R-3m		R_{wp}=2.20%		
Atom	x	y	z	Occupancy	Uiso
Li1	0.0	0.0	0.500	0.9760	0.01379
Ni1	0.0	0.0	0.0	0.8073	0.00279
Co1	0.0	0.0	0.0	0.1172	0.00279
Mn1	0.0	0.0	0.0	0.0499	0.00279
Al1	0.0	0.0	0.0	0.0016	0.00279
O1	0.0	0.0	0.255	0.9402	0.00330
N1	0.0	0.0	0.255	0.0598	0.00330
Li2	0.0	0.0	0. 0	0.0240	0.00279
Ni2	0.0	0.0	0.500	0.0240	0.01379

Table S7. The area of the total DOS in the highlighted area in Figure S12e.

Model	NiO	$NiO_{0.94}N_{0.06}$	$NiO_{0.88}N_{0.12}$
Area	4.9664	5.0485	13.5000

Table S8. The electronic conductivity of pristine NCM83, water-washed NCM83, NCM83-Al, and NCM83-Al-N.

Cathodes	Electronic conductivity (S cm^{-1})
Pristine NCM83	0.0062
Water-washed NCM83	0.0067
NCM83-Al	0.0088
NCM83-Al-N	0.0121

It is noted that the electronic conductivity for NCM83-Al is lower than that of NCM83-Al-N may be because the thicker Al_2O_3 layer on the surface of NCM83-Al.

Table S9. EIS data obtained by fitting Nyquist plots using the equivalent circuit in Figure S18.

Electrodes	Cycle number	R_{SEI} (Ω)	R_{ct} (Ω)
Pristine NCM83	0th	42.23	236.7
	50th	75.51	305.2
	100th	146.2	452.3
	200th	924.7	957.6
Water-washed NCM83	0th	122.8	157.4
	50th	193.8	459.3
	100th	207.0	951.8
	200th	1125	1219
NCM83-Al	0th	39.45	179.2
	50th	162.1	254.5
	100th	176.1	381.9
	200th	185.6	670.7
NCM83-Al-N	0th	15.34	97.1
	50th	107.7	138.4
	100th	149.5	244.5
	200th	164.3	256.7

References

1. F. Li, Z. Liu, C. Liao, X. Xu, M. Zhu, and J. Liu, *ACS Energy Letters*, 2023, **8**, 4903-4914.
2. G. Kresse and J. Furthmüller, *Computational Materials Science*, 1996, **6**, 15-50.
3. G. Kresse and J. Furthmüller, *Physical Review B*, 1996, **54**, 11169-11186.
4. P. E. Blöchl, *Physical Review B*, 1994, **50**, 17953-17979.
5. J. P. Perdew, J. A. Chevary, S. H. Vosko, K. A. Jackson, M. R. Pederson, D. J. Singh and C. Fiolhais, *Physical Review B*, 1992, **46**, 6671-6687.
6. S. Grimme, J. Antony, S. Ehrlich and H. Krieg, *The Journal of Chemical Physics*, 2010, **132**.
7. J. P. Perdew, K. Burke and M. Ernzerhof, *Physical Review Letters*, 1996, **77**, 3865-3868.
8. A. Floris, S. de Gironcoli, E. K. U. Gross and M. Cococcioni, *Physical Review B*, 2011, **84**.
9. S. L. Dudarev, G. A. Botton, S. Y. Savrasov, C. J. Humphreys and A. P. Sutton, *Physical Review B*, 1998, **57**, 1505-1509.
10. F. Kong, C. Liang, L. Wang, Y. Zheng, S. Perananthan, R. C. Longo, J. P. Ferraris, M. Kim and K. Cho, *Advanced Energy Materials*, 2018, **9**.
11. L. Wang, T. Maxisch and G. Ceder, *Physical Review B*, 2006, **73**.